

See discussions, stats, and author profiles for this publication at: <https://www.researchgate.net/publication/337526871>

Change of El Niño and La Niña amplitude asymmetry around 1980

Article in *Climate Dynamics* · February 2020

DOI: 10.1007/s00382-019-05062-y

CITATIONS

0

READS

212

3 authors:



Xiao Pan

Nanjing University of Information Science & Technology

5 PUBLICATIONS 1 CITATION

[SEE PROFILE](#)



Tim Li

University of Hawai'i System

385 PUBLICATIONS 14,549 CITATIONS

[SEE PROFILE](#)



Mingcheng Chen

Nanjing University of Information Science & Technology

7 PUBLICATIONS 79 CITATIONS

[SEE PROFILE](#)

Some of the authors of this publication are also working on these related projects:



Model convergence in simulating tropical cyclone intensity in high-resolution model [View project](#)



Impact of global warming on tropical cyclone activity [View project](#)



Change of El Niño and La Niña amplitude asymmetry around 1980

Xiao Pan¹ · Tim Li^{1,2} · Mingcheng Chen¹

Received: 2 April 2019 / Accepted: 18 November 2019
© Springer-Verlag GmbH Germany, part of Springer Nature 2019

Abstract

Amplitude of El Niño and La Niña was significantly different during 1980–2016 but almost same during 1958–1979. The cause of this interdecadal change is investigated through an oceanic mixed-layer heat budget analysis. It was found that this interdecadal change was primarily attributed to the distinctive effects of nonlinear zonal temperature advection between the two periods. During 1980–2016 nonlinear zonal advection, working together with nonlinear meridional advection, contributes to the El Niño and La Niña amplitude asymmetry. During 1958–1979 the nonlinear zonal advection had an opposite effect. The difference in the nonlinear zonal advection between the two interdecadal periods was caused by distinctive longitudinal locations of El Niño centers. Maximum SST anomaly (SSTA) centers were confined near the coast of South America (east of 90° W) during the first period but appear near 110° W during the second period. Because of this difference, an anomalous eastward ocean surface current (caused by a positive thermocline depth anomaly during El Niño) would generate a negative (positive) nonlinear zonal advection before (after) 1980. The distinctive longitudinal locations of El Niño centers are possibly caused by the interdecadal changes of mean thermocline and high-frequency wind variability over the equatorial western-central Pacific. A hypothesis was put forth to understand distinctive initiation locations between El Niño and La Niña.

Keywords El Niño and La Niña amplitude asymmetry · Interdecadal change · Nonlinear advection · El Niño initiation location · Mean thermocline change · Westerly wind events

1 Introduction

As a dominant interannual mode in the tropics, the El Niño–Southern Oscillation (ENSO) involves strong coupling between the atmosphere and ocean and has a great impact on climate worldwide (e.g., Ropelewski and Halpert 1987; Huang and Wu 1989; Bove et al. 1998; Changnon 1999; McPhaden et al. 2006; see a review on fundamental ENSO dynamics by Li and Hsu 2017). Previous studies investigated

how remote sea surface temperature anomaly (SSTA) in the tropical Pacific influenced the climate in mid- and high- latitudes. For example, ENSO can directly affect the climate in North America in northern winter via the “Pacific–North America” (PNA) pattern (Wallace and Gutzler 1981), or indirectly affect North American rainfall in boreal summer through a so called “Asia–North America” pattern (Zhu and Li 2016, 2018). ENSO also exerted a delayed impact on summer rainfall in East Asia via the development and maintenance of an anomalous anticyclone over western North Pacific (WNP) (e.g., Wang et al. 2000, 2003; Wu et al. 2010, 2017; Li et al. 2017).

Previous observational, theoretical and modeling studies have laid foundation for understanding ENSO coupled air–sea instability (e.g., Rasmusson and Carpenter 1982; Philander et al. 1984), oscillatory behavior (e.g., Cane and Zebiak 1985; Suarez and Schopf 1988; Battisti and Hirst 1989; Jin 1997; Li 1997; Weisberg and Wang 1997; Picaut et al. 1997; Neelin et al. 1998) and phase locking characteristic (e.g., Chang et al. 1994; Li 1997). An interesting feature is amplitude asymmetry between El Niño and La Niña. During the past 3–4 decades, the amplitude of El Niño

✉ Tim Li
timli@hawaii.edu

¹ Key Laboratory of Meteorological Disaster, Ministry of Education (KLME)/Joint International Research Laboratory of Climate and Environmental Change (ILCEC)/ Collaborative Innovation Center on Forecast and Evaluation of Meteorological Disasters (CIC-FEMD), Nanjing University of Information Science and Technology, Nanjing, China

² Department of Atmospheric Sciences, International Pacific Research Center, School of Ocean and Earth Science and Technology, University of Hawaii at Manoa, Honolulu, HI 96822, USA

was often stronger than that of La Niña. Burgers and Stephenson (1999) showed that positive skewness of the SSTA mainly appeared in the eastern equatorial Pacific. Jin et al. (2003), An and Jin (2004) and An et al. (2005) found that the ENSO amplitude asymmetry was caused by nonlinear vertical temperature advection. But this result was questioned by Su et al. (2010), who demonstrated through analyzing multiple ocean reanalysis datasets that nonlinear horizontal advection was essential in causing the asymmetry while nonlinear vertical advection plays an opposite role. Su et al. (2010) further indicated that the discrepancy between them lies in oceanic vertical velocity bias in the test version of SODA data used by Jin et al. (2003), An and Jin (2004) and An et al. (2005).

The El Niño and La Niña amplitude asymmetry may closely relate to their evolution asymmetry. For example, Okumura and Deser (2010) suggested that the asymmetry could arise from the asymmetry of duration of warm and cold ENSO events, as El Niño life span is much shorter than that of La Niña (Wu et al. 2010). A heat budget analysis indicated that such an evolution asymmetry arose from both asymmetric wind stress and heat flux impacts (Chen et al. 2016c). It is, however, not clear whether the asymmetric circulation and heat flux patterns were caused by the amplitude asymmetry.

It was suggested that there might be a two-way interaction between ENSO and the mean state. On the one hand, the interdecadal change of the Pacific mean state such as Pacific Decadal Oscillation (PDO) could greatly modulate the ENSO behavior (e.g., Kirtman and Schopf 1998; Choi et al. 2009; Xiang et al. 2013; Chung and Li 2013; Yeo et al. 2016; Okumura et al. 2017; Li et al. 2019). On the other hand, the change of the mean state could be influenced by nonlinear rectification of ENSO (e.g., Rodgers et al. 2004; Yeh and Kirtman 2004). Besides the PDO, Atlantic Multi-decadal Oscillation (AMO) could modulate ENSO variability (e.g., Dong et al. 2006; Kang et al. 2014). Global warming induced mean climate change could significantly modulate ENSO feedback processes (e.g., Collins et al. 2010; Cai et al. 2014; Chen et al. 2015, 2017a).

The current study was motivated by observational fact that El Niño and La Niña amplitude asymmetry underwent an interdecadal change (e.g., Wang and An 2001; An 2004). What caused such an interdecadal change is still an open issue. As shown in Sect. 3, El Niño and La Niña amplitude asymmetry was statistically significant after 1980, but became insignificant during 1958–1979. The objective of the current study is to reveal the fundamental cause of this interdecadal change. The remaining part of this paper is organized as following. In Sect. 2, data and methods are introduced. In Sect. 3, the observed evolution characteristics of El Niño and La Niña amplitude asymmetry since 1958 are examined. Ocean mixed layer heat budgets prior to and

after 1980 are diagnosed, and the cause of the amplitude asymmetry is examined in Sect. 4. A further discussion on key issues about interdecadal change of ENSO amplitude asymmetry is given in Sect. 5. Finally, a conclusion is given in the last section.

2 Data and analysis method

2.1 Data

The SST field used in this study is from the Extended Reconstructed Sea Surface Temperature version 3b (ERSST.v3b; Xue et al. 2003; Smith et al. 2008). It has a resolution of $2^\circ \times 2^\circ$, and covers the period of 1854 to present. For the current study, we focus on our analysis to the period from 1958 to 2016. In addition, three-dimensional ocean current and temperature fields and surface height fields are used and they are obtained from Simple Ocean Data Assimilation version 2.2.4 (SODAv2.2.4; Carton et al. 2000; Carton and Giese 2008) and the National Center for Environmental Prediction (NCEP) Global Ocean Data Assimilation system (GODAS; Behringer 2007) products. Oceanic thermocline depth fields (20°C isotherm depth) are obtained indirectly from SODAv2.2.4 and GODAS. SODAv2.2.4 product has a horizontal resolution of $0.5^\circ \times 0.5^\circ$ and 40 vertical levels with 10-m resolution in the upper 100 m. GODAS product has 1° in zonal and $1/3^\circ$ in meridional resolution and 40 vertical levels with 10-m resolution in the upper 200 m. Considering that mixed-layer heat budget result might be sensitive to ocean reanalysis data (Huang et al. 2010), a comparison has been done for the budget with and without the use of GODAS. The result is not sensitive. Both the SODA and GODAS products have been used in a number of previous ENSO studies (e.g., Chen et al. 2016a, b).

The surface heat flux fields are taken from various datasets for different periods, including Earth System Research Laboratory Twentieth Century Reanalysis version 2c (20CRv2c; Compo et al. 2006), National Center for Environmental Prediction Reanalysis version 2 (NCEP2; Kanamitsu et al. 2002) and European Center for Medium-Range Weather Forecasts (ECMWF) Re-Analysis data (ERA-Interim; Dee et al. 2011). The 20CRv2c and NCEP2 products have the resolution of about 2° in meridional direction and 1.875° in zonal direction, while the ERA-Interim data has a $1^\circ \times 1^\circ$ resolution.

Given the uncertainty in the reanalysis products (e.g., Kumar and Hu 2012), we use the ensemble average of the three reanalysis heat flux datasets (NCEP2, ERA-Interim and 20C-v2) for mixed-layer heat budget analysis. A comparison of composite heat flux anomalies for El Niño and La Niña between the ensemble average product and the OAF flux dataset for the period of 1984–2009 was carried out, and the result

shows that they are quite similar (figure not shown). This adds the confidence to use the ensemble mean product.

The daily atmospheric wind fields and wind stress fields are taken from the 40-year ECMWF Re-Analysis (ERA40) data (Uppala et al. 2005) and ERA-Interim. Both ERA40 and ERA-Interim data have a horizontal resolution of $1^\circ \times 1^\circ$ and 12 vertical levels. All data above are interpolated into $1^\circ \times 1^\circ$ grid prior to analysis.

2.2 Method

To investigate the relative contributions of ocean 3-dimensional advection terms and surface heat flux terms in causing the asymmetric SSTA tendency between El Niño and La Niña group, an oceanic mixed-layer heat budget is diagnosed. Following previous studies (Li et al. 2002; Chen et al. 2015, 2017a, 2019), the mixed-layer temperature anomaly (MLTA) tendency equation may be written as follows:

$$\begin{aligned} \frac{\partial T'}{\partial t} = & - \left(\bar{u} \frac{\partial T'}{\partial x} + u' \frac{\partial \bar{T}}{\partial x} + u' \frac{\partial T'}{\partial x} \right) - \left(\bar{v} \frac{\partial T'}{\partial y} + v' \frac{\partial \bar{T}}{\partial y} + v' \frac{\partial T'}{\partial y} \right) \\ & - \left(\bar{w} \frac{\partial T'}{\partial z} + w' \frac{\partial \bar{T}}{\partial z} + w' \frac{\partial T'}{\partial z} \right) + \frac{Q'_{net}}{\rho C_p H} + R \end{aligned} \tag{1}$$

where T denotes mixed-layer temperature, u, v, w represent 3D mixed-layer current velocity, a prime denotes the interannual anomaly field, a bar represents the climatological mean annual cycle field, Q'_{net} denotes the net surface heat flux anomaly that includes anomalous longwave radiation, shortwave radiation, latent heat flux and sensible heat flux, $\rho = 1015 \text{ kg m}^{-3}$ denotes the density of water, $C_p = 4000 \text{ J kg}^{-1} \text{ K}^{-1}$ is the specific heat of water, and $H = 30 \text{ m}$ denotes a constant climatological mixed-layer depth in the eastern equatorial Pacific. The climatological annual cycle mean state is calculated based on the period of 1958–1979 and 1980–2016 respectively. The anomaly field is calculated by subtracting original monthly mean field from its climatological annual cycle at each period respectively. The mixed-layer heat budget analysis results are based on the ensemble average of SODAv2.2.4 and GODAS, whereas the atmospheric fields are plotted according to the ensemble average of three reanalysis datasets, 20CRv2c, NCEP2 and ERA-Interim.

Skewness is used to measure the asymmetry of a probability distribution function and 0 is for a normal distribution (White 1980). The skewness is defined as:

$$skewness = m_3 / (m_2)^{\frac{3}{2}} \tag{2}$$

where $m_k = \frac{1}{N} \sum_{i=1}^N (x_i - \bar{x})^k$, \bar{x} denotes the long-term climatological mean value; m_k is the k th moment, x_i is the i th observation and N is the number of observations. A positive skewness implies that a positive anomaly is greater than a

negative anomaly. To examine whether or not a positive or negative skewness is statistically significant, a range estimate method following Hong et al. (2008) and Su et al. (2010) was applied. For the current sample length, a confidence level of 95% corresponds to the amplitude of the skewness exceeding ± 0.67 (Su et al. 2010).

The Mann–Kendall test (MK test) method is used to test whether there is a significant change in a time series. The specific mathematical description is as follows.

Suppose there is a time series (Y_1, Y_2, \dots, Y_n) . Let m_i represent the cumulative number of i th sample Y_i that is greater than Y_j ($1 \leq j \leq i$). Define d_k as following:

$$d_k = \sum_1^k m_i, (2 \leq k \leq n)$$

Assume that the original sequence is random series. The mean and variance of d_k can be expressed as

$$E(d_k) = \frac{k(k-1)}{4}, \text{ var}(d_k) = \frac{k(k-1)(2k+5)}{72}$$

By standardizing d_k , a new function (UF_k) can be obtained:

$$UF_k = \frac{d_k - E(d_k)}{\sqrt{\text{var}(d_k)}}$$

Function UF_k forms a UF curve. It can be used to test whether or not the original series has a significant trend. Applying this method to the inverse sequence, one may obtain another curve UB. The intersection of the two curves (UF and UB) within a significance interval indicates that there is a changing point at this intersection. Given a significance level of $\alpha = 0.05$, the threshold values for UF and UB are ± 1.96 . If $UF > 0$, the sequence has an increasing trend; otherwise, it has a decreasing trend. The trend is significant when UF is greater than 1.96 or less than -1.96 .

3 Observed evolution characteristics of ENSO amplitude asymmetry

The time series of observed monthly SST anomaly averaged in Niño-3 region is shown in Fig. 1. Note that before 1980, the amplitude of El Niño and La Niña was approximately same, whereas after 1980 the amplitude of El Niño was obviously stronger than that of La Niña. The Mann–Kendall test (MK test) method is used to test whether there is a significant change point in the time series of Niño-3 index. Figure 2 shows the test result. It is clearly seen that an intersection of the UB and UF curves appears in 1979. This implies that a significant changing point happened in 1979. Therefore, we define

two interdecadal periods, 1958–1979 (hereafter ID1) and 1980–2016 (hereafter ID2), in an attempt to investigate the characteristics and physical cause of El Niño and La Niña amplitude asymmetry between the two periods.

In this study ENSO cases were defined as 3-month mean SSTA averaged over Niño-3 region being greater than 0.5°C (less than -0.5°C) for five consecutive overlapping seasons. As shown in Fig. 1, the developing phases of selected El Niño and La Niña cases are indicated by a color bar with red representing the developing phase of El Niño and blue representing the developing phase of La Niña. A crude measure of the El Niño and La Niña amplitude asymmetry is the average of the Niño-3 Index in December for all El Niño and La Niña events for ID1 and ID2. The result is shown by green line in Fig. 1. The average value is -0.12°C in ID1 and 0.71°C in ID2, implying that the amplitude of La Niña

is slightly stronger in the former period but the amplitude of El Niño is much greater than La Niña in the latter period.

A better measure of the amplitude asymmetry is to calculate the skewness of monthly SSTA for each of the periods. Figure 3 shows that the skewness is in general small and negative along the equatorial Pacific during ID1 but became significantly larger and positive during ID2, in particular over the eastern equatorial Pacific. The result indicates that the amplitude of El Niño is significantly stronger than that of La Niña during ID2 but the amplitude asymmetry became insignificant during ID1.

Following Wu et al. (2010), the asymmetric (symmetric) component of the skewness fields between the two periods is obtained by adding (subtracting) the two skewness fields. Maximum asymmetry appears over the region between 5°S and 5°N , 110°W and 80°W . In the subsequent mixed layer

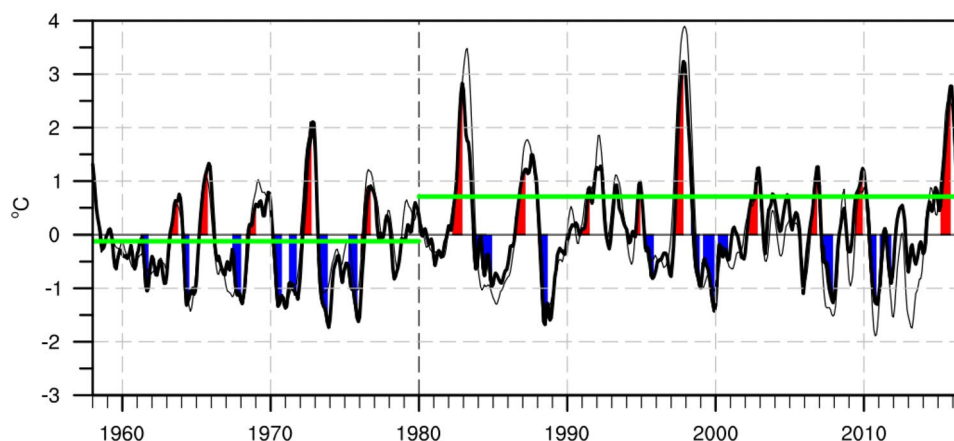
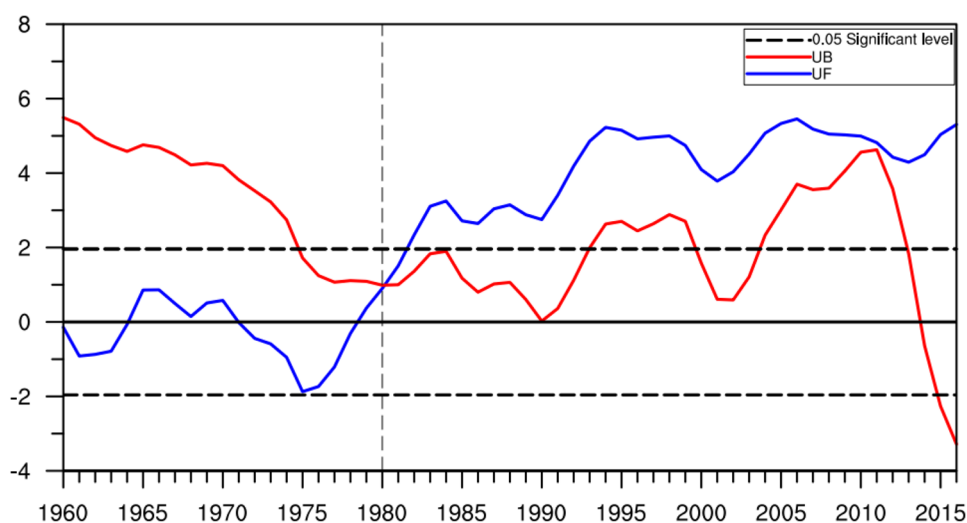


Fig. 1 Time series of sea surface temperature anomaly (SSTA) in Niño-3 region with 3-month mean (thick black line) and mixed-layer temperature anomaly (MLTA) in the equatorial eastern Pacific region (5°S – 5°N , 110° – 80°W ; light black line) with 7-month running mean during 1958–2016. The thick green line denotes the difference

(unit: $^{\circ}\text{C}$) of average El Niño amplitude and average La Niña amplitude (defined as Niño-3 index in December) in ID1 and ID2 respectively. The developing phase for each El Niño (La Niña) case is indicated by a red (blue) bar

Fig. 2 Mann–Kendall test of Niño-3 Index (unit: $^{\circ}\text{C}$) during 1960–2016. The red line is UB and the blue line is UF. The 0.05 significant level is indicated by two black dotted lines



heat budget analysis, we will focus on our diagnosis in this maximum asymmetry region. From Fig. 1, one can see that the time series of MLTA is quite similar to that of the SSTA. This implies that the result derived from the mixed layer heat budget can be used to interpret the SSTA change.

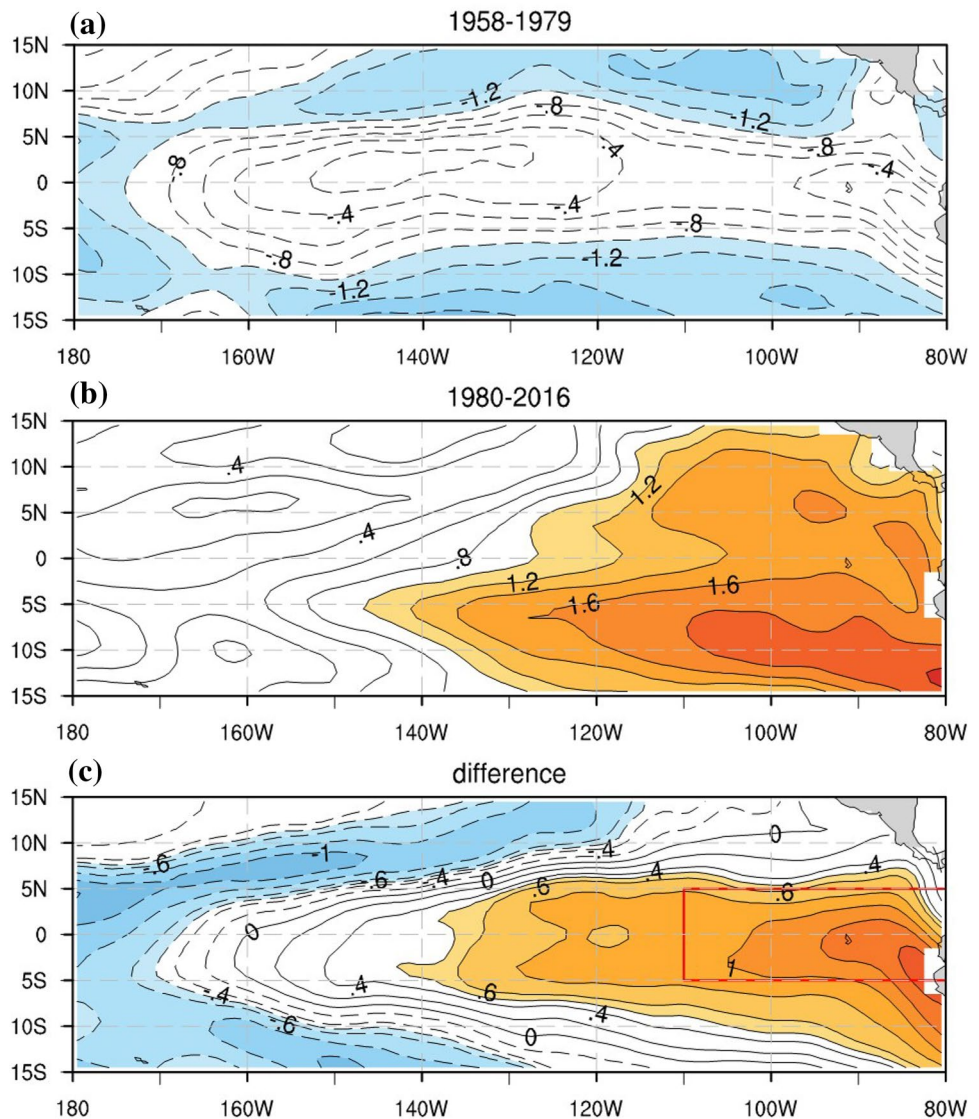
4 Cause of interdecadal change of ENSO amplitude asymmetry—a Mixed-layer heat budget diagnosis

The oceanic mixed layer heat budget is diagnosed in the key analysis region (5°S – 5°N , 110°W – 80°W) during the developing phases of El Niño and La Niña for ID1 and ID2 respectively. Figure 4 shows the contributions from individual dynamic and thermodynamic terms for El Niño and

La Niña composites at each period. The overall budget is reasonable and residual terms are relatively small.

Both the observed and diagnosed MLTA tendencies show that they are almost same for El Niño and La Niña composite during ID1 but quite different during ID2. This indicates that the mixed layer heat budget analysis adequately captures the amplitude symmetry (asymmetry) in ID1 (ID2), being consistent with the observed SSTA evolution characteristic. The cause of the MLTA tendency asymmetry, as seen from Fig. 4, is primarily attributed to 3-dimensional temperature advection terms, as heat flux terms tend to offset the advection effect. For example, during ID2, the sum of advection terms is $0.41\text{ }^{\circ}\text{C month}^{-1}$ for El Niño and $-0.26\text{ }^{\circ}\text{C month}^{-1}$ for La Niña, while the heat flux term is $-0.14\text{ }^{\circ}\text{C month}^{-1}$ for El Niño and $0.08\text{ }^{\circ}\text{C month}^{-1}$ for La Niña. A stronger positive contribution of the advection favors a stronger El Niño, while a stronger negative contribution of the heat flux

Fig. 3 Distribution of skewness in the period of **a** 1958–1979 and **b** 1980–2016 within (15°S – 15°N , 180° – 80°W), shading denotes the value exceeding a confidence level of 95% using t test. **c** is the sum of (**a**, **b**)



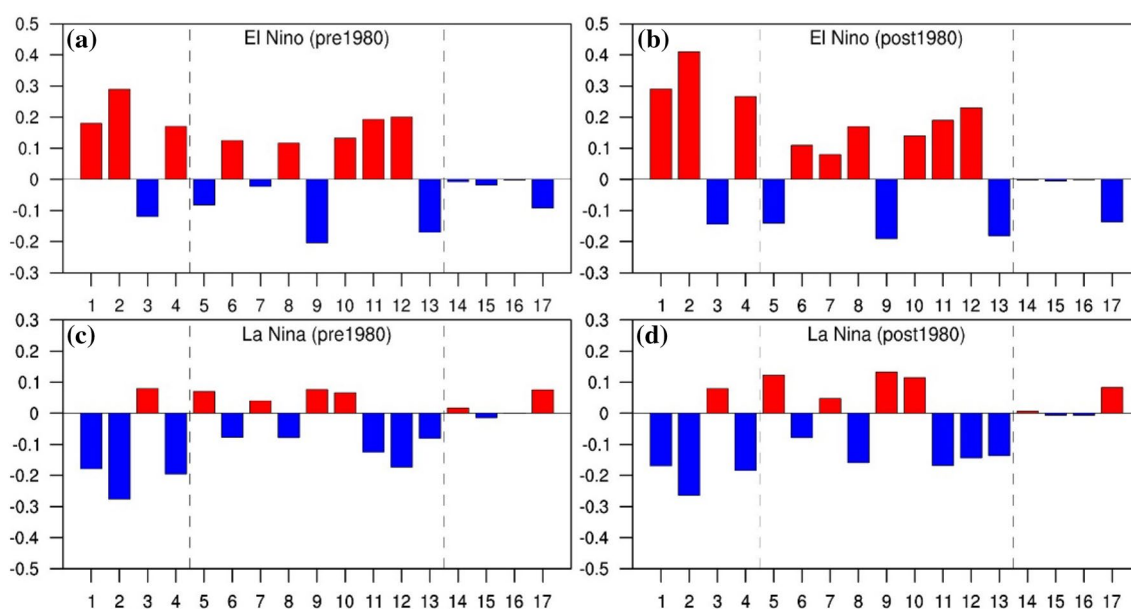


Fig. 4 The diagnosed results of mixed-layer heat budget, terms (left–right) along the x axis: the mixed-layer temperature anomaly tendency, the sum of temperature advection term, the sum of surface heat flux, the sum of the advection term and surface flux term, $-\bar{u} \frac{\partial T'}{\partial x}$, $-u' \frac{\partial T'}{\partial x}$, $-\bar{v} \frac{\partial T'}{\partial y}$, $-v' \frac{\partial T'}{\partial y}$, $-\bar{w} \frac{\partial T'}{\partial z}$, $-w' \frac{\partial T'}{\partial z}$, anomalous longwave radiation, anomalous shortwave radiation, anomalous sensible heat flux, anomalous latent heat flux (unit:

$^{\circ}\text{C month}^{-1}$). The calculation is based on SODAv2.2.4 and GODAS. Red and blue bars represent results for positive terms and negative terms, respectively. All the terms are averaged over the far eastern equatorial Pacific ($5^{\circ}\text{ S} - 5^{\circ}\text{ N}$, $110^{\circ} - 80^{\circ}\text{ W}$), 30 m depth for the developing phases. **a** 1958–1979 of El Niño composites; **b** 1980–2016 of El Niño composites; **c** 1958–1979 of La Niña composites; **d** 1980–2016 of La Niña composites

favors a weaker El Niño. The overall MLTA tendency is dominated by the advection term.

Next we focus on examining the role of individual advection terms. Following Su et al. (2010), the temperature advection term is decomposed into nine terms (for details about these terms, readers are referred to Eq. 1). Each of zonal, meridional and vertical advection consists of three terms, two linear terms and one nonlinear term. Figure 5 shows the diagnosis result for sum of linear and nonlinear advection terms. Note that during ID2 the nonlinear advection is positive for both El Niño and La Niña, while the linear advection has a similar value but an opposite sign. Adding the nonlinear term to the linear term leads to a stronger (weaker) MLTA tendency for El Niño (La Niña). This indicates that the nonlinear advection is essential to cause the amplitude asymmetry. This result is consistent with Su et al. (2010).

Interestingly, the nonlinear advection behaved differently during ID1. It is negative (positive) during El Niño (La Niña), and tends to suppress the linear advection effect for both El Niño and La Niña. As a result, El Niño and La Niña tendencies during the period were approximately symmetric.

Comparing the nonlinear advection terms between ID1 and ID2 (as shown in Fig. 5a, b), one can see clearly that the difference is mainly caused by the difference during El Niño. The terms are almost same during La Niña. To reveal

the cause of the difference between ID1 and ID2 during El Niño, we further examine individual nonlinear advection terms during ID1 and ID2 and the result is shown in Fig. 5c. Note that the main difference lies in nonlinear zonal temperature advection. It contributes negatively to the MLTA tendency during ID1 and changes to a positive contribution during ID2. The nonlinear meridional and vertical temperature advection terms are almost same during ID1 and ID2. In contrast, three individual nonlinear advection terms always kept the same sign for ID1 and ID2 during La Niña (Fig. 5d). Therefore, it is concluded that the nonlinear zonal temperature advection plays a critical role in causing the interdecadal change of El Niño and La Niña amplitude asymmetry.

What causes the change of nonlinear zonal temperature advection? To address the question, we plotted the horizontal patterns of composite anomalous mixed-layer horizontal currents (u' , v'), MLTA and SSTA (Fig. 6). Here the mixed-layer depth is defined as where the temperature is 0.5° C lower than surface temperature. A common feature between ID1 and ID2 is eastward (westward) ocean surface current anomaly along the equator for El Niño (La Niña). The main difference lies in the longitudinal locations of maximum positive SSTA/MLTA center denoted by green dots in Fig. 6a, b. During ID1, the maximum SSTA/MLTA center of El Niño is located near the coast of South America (east of 90° W). During ID2, the center of the maximum SSTA appears at 115° W , a

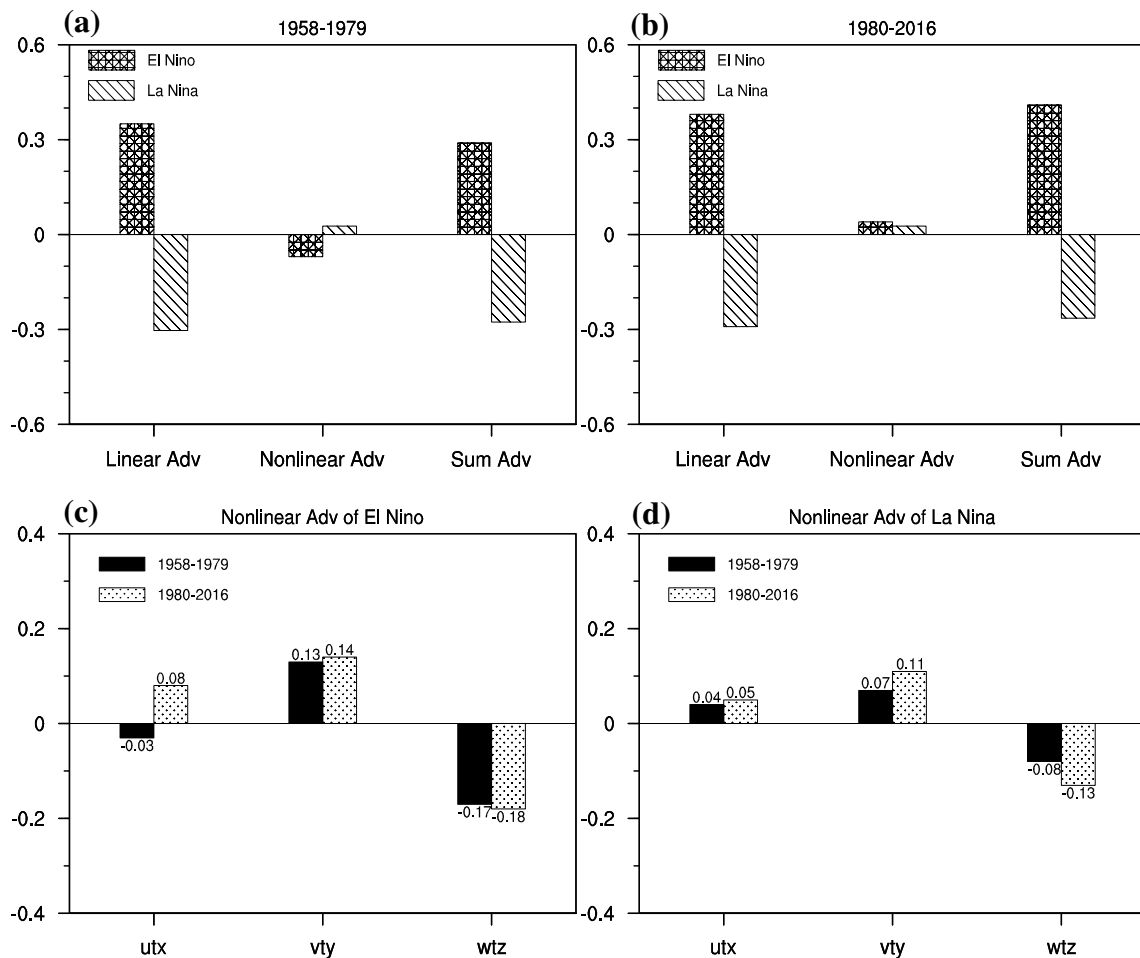


Fig. 5 Linear advection, nonlinear advection and sum of linear and nonlinear advection terms of mixed layer heat budget during the developing phase of El Niño and La Niña for the period of **a** 1958–

1979 and b 1980–2016. Nonlinear zonal, meridional and vertical advection terms during the **c** El Niño and **d** La Niña developing phase for the period of 1958–1979 and 1980–2016

westward shifting of 30° in longitude. As a result, a negative (positive) zonal nonlinear advection anomaly appears in the green box (shown in Fig. 6a, b) during ID1 (ID2).

In contrast, maximum negative SSTA centers are always located near the western boundary of the eastern equatorial Pacific box during La Niña (Fig. 6c, d). Because of that, anomalous zonal temperature advection keeps the same sign (i.e., positive) for ID1 and ID2. This leads to positive nonlinear zonal advection for both the periods, weakening the amplitude of La Niña.

To sum up, the nonlinear zonal advection term ($-u' \frac{\partial T'}{\partial x}$) is negative (positive) during El Niño (La Niña) prior to 1980. This weakens the amplitude of both El Niño and La Niña. After 1980, the nonlinear zonal temperature advection is positive in both El Niño and La Niña, which tends to enhance the amplitude of El Niño but suppress the amplitude of La Niña. Given that nonlinear meridional and vertical advection terms are essentially same, the interdecadal change of nonlinear zonal temperature advection

holds a key in determining the change of the El Niño and La Niña amplitude asymmetry characteristic.

The eastward ocean surface current anomaly during El Niño (as shown in Fig. 6a) cannot be explained by surface zonal wind stress anomaly alone (Su et al. 2010). To address this issue, we separate anomalous zonal current into wind-induced Ekman current and geostrophic current following Su et al. (2010):

$$u' = u'_g + u'_e \tag{3}$$

$$v' = v'_g + v'_e \tag{4}$$

$$u'_g = -\frac{g'}{\beta} \frac{\partial^2 h'}{\partial y^2}, \quad v'_g = \frac{g'}{\beta} \frac{\partial^2 h'}{\partial x \partial y} \tag{5}$$

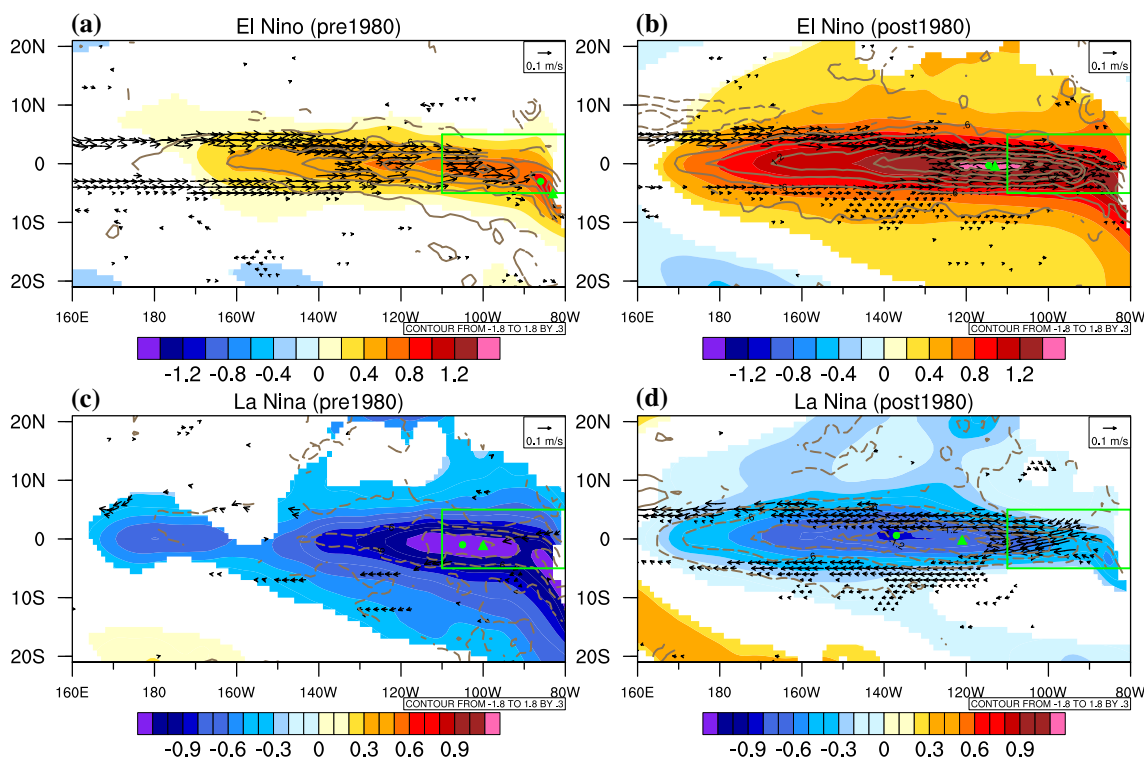


Fig. 6 Composite SSTA (shading; unit: °C), MLTA (contour; unit: °C) and anomalous horizontal currents (vector; unit: m s⁻¹) of El Niño (top panels) and La Niña (bottom panels). The left panels are El Niño (top panel) and La Niña (bottom panel) in 1958–1979 respec-

tively, and right is in 1980–2016. Green line box indicates the diagnosed box. The green dot and triangle denote the maximum (minimum) SSTA and MLTA center of El Niño (La Niña). Variables that pass the 90% bootstrap significance level are shown

$$u'_e = \frac{1}{\rho H_1} \frac{r_s \tau'_x + \beta y \tau'_y}{r_s^2 + (\beta y)^2}, \quad v'_e = \frac{1}{\rho H_1} \frac{r_s \tau'_y - \beta y \tau'_x}{r_s^2 + (\beta y)^2} \quad (6)$$

where ρ denotes the density of seawater, H_1 is the mean thermocline depth, τ'_x and τ'_y is anomalous zonal and meridional wind stress, $r_s = 0.5 \text{ day}^{-1}$ is a dissipation coefficient, $g' = 0.026 \text{ m s}^{-1}$ is the reduced gravity, h' is the thermocline depth anomaly represented by 20 °C isotherm depth anomaly, and β is the planetary vorticity.

Our diagnosis result shows that the anomalous zonal current at the equator is dominated by geostrophic current component while Ekman current component is negligible (shown in Fig. 7). According to Eq. (5), anomalous geostrophic current is determined by thermocline depth anomaly. During El Niño developing phase, the thermocline depth in the equatorial central and eastern Pacific is deepened and there is a maximum center of thermocline depth anomaly at the equator. This leads to $\frac{\partial^2 h'}{\partial y^2} < 0$ and thus a positive geostrophic current ($u'_g > 0$). Conversely, the thermocline depth in the equatorial central and eastern Pacific becomes shallower during La Niña. According to Eq. (5), a minimum center of thermocline depth anomaly contributes to a negative geostrophic current anomaly ($u'_g < 0$).

It is important to note that the interdecadal change of nonlinear zonal advection depends on the change of anomalous SSTA pattern associated with El Niño. While the maximum SSTA center is near the American coast during ID1, it shifted westward to 115° W during ID2. What caused such a shift? Figure 8 illustrates the evolution of the SSTA and MLTA patterns during El Niño developing phase (from April to September) for both the periods. It is interesting to note that in ID1, a warm SSTA starts to develop from the American coast (around 85° W) (Fig. 8a). As it develops, the SSTA center shifts slightly westward and is primarily confined over the region east of 90° W (Fig. 8b, c). In contrast, in ID2 a maximum SSTA center forms in the central Pacific (around 170° W) (Fig. 8d). It then shifts eastward in the following months as it develops (Fig. 8e–f). During the entire developing phase, the maximum SSTA remains west of 110° W. Thus, the distinctive initial warming characteristics may determine the subsequent location of the maximum SSTA center.

In contrast, initial cooling characteristics during La Niña are different from those of El Niño. Figure 9 shows the composite La Niña SSTA evolution patterns during the two interdecadal periods. It is interesting to note that the cold anomalies

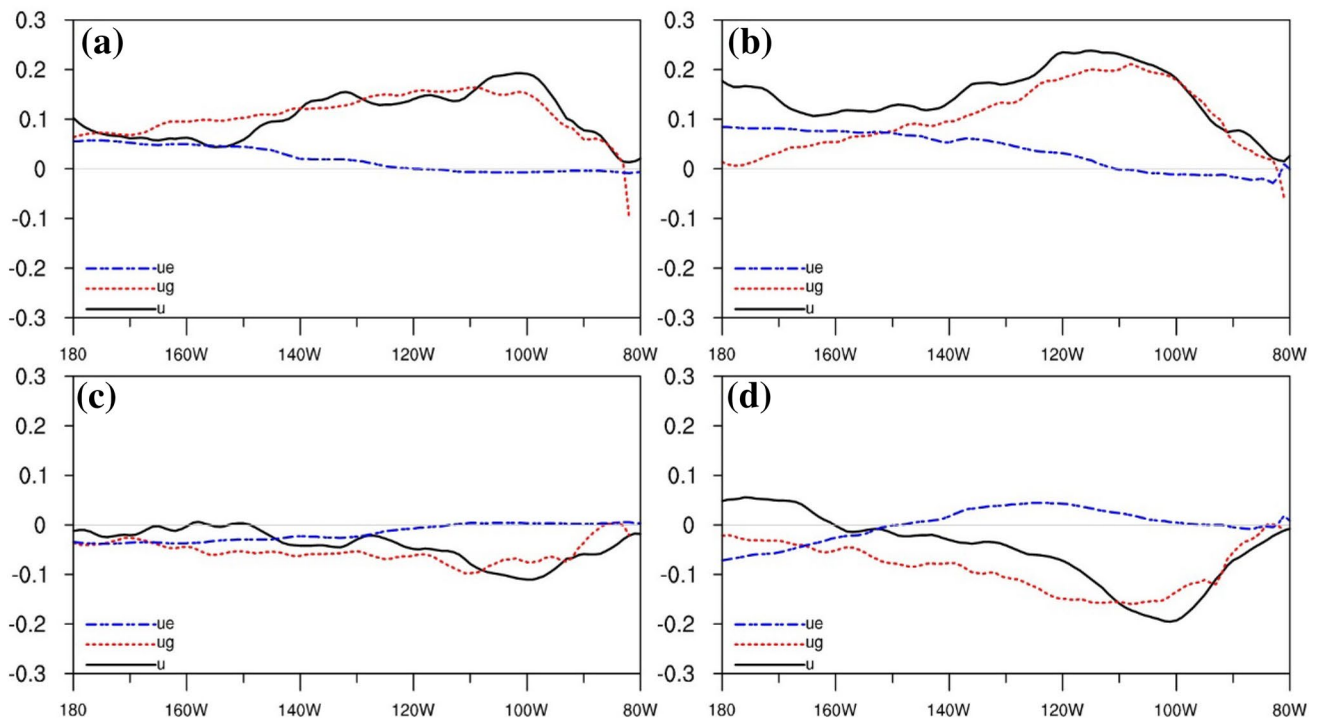


Fig. 7 Anomalies of zonal currents (black solid line; unit: $m s^{-1}$), geostrophic currents (red dotted line; unit: $m s^{-1}$) and Ekman currents (blue dashed line; unit: $m s^{-1}$) along the equator (within $\pm 2^\circ$) during the developing phase of El Niño (top panels) and La Niña

(bottom panels). The left panels are composite El Niño (top panel) and La Niña (bottom panel) in 1958–1979 respectively, and right is in 1980–2016

associated with La Niña always move eastward, with maximum cooling centers being confined west of $110^\circ W$.

5 Discussion: what controls the distinctive characteristics of El Niño initiation location between the two interdecadal periods?

In the previous section, we demonstrate that initial warming locations for El Niño are different between ID1 and ID2. What causes the distinctive El Niño initiation characteristics between ID1 and ID2? We speculate that it may be partially controlled by the interdecadal change of the Pacific mean state. Figure 10 illustrates the mean SST, 850 hPa wind and thermocline depth change between ID1 and ID2. An interdecadal warming leads to enhanced trade wind at the equator (Fig. 10a). The wind stress curl further causes the shoaling of equatorial thermocline through Sverdrup transport (Li 1997). SODAv2.2.4 and GODAS show a shallower mean thermocline depth in ID2 than ID1 (Fig. 10b).

The Sverdrup relationship between the zonal mean wind stress curl and zonal mean meridional current can be written as follows:

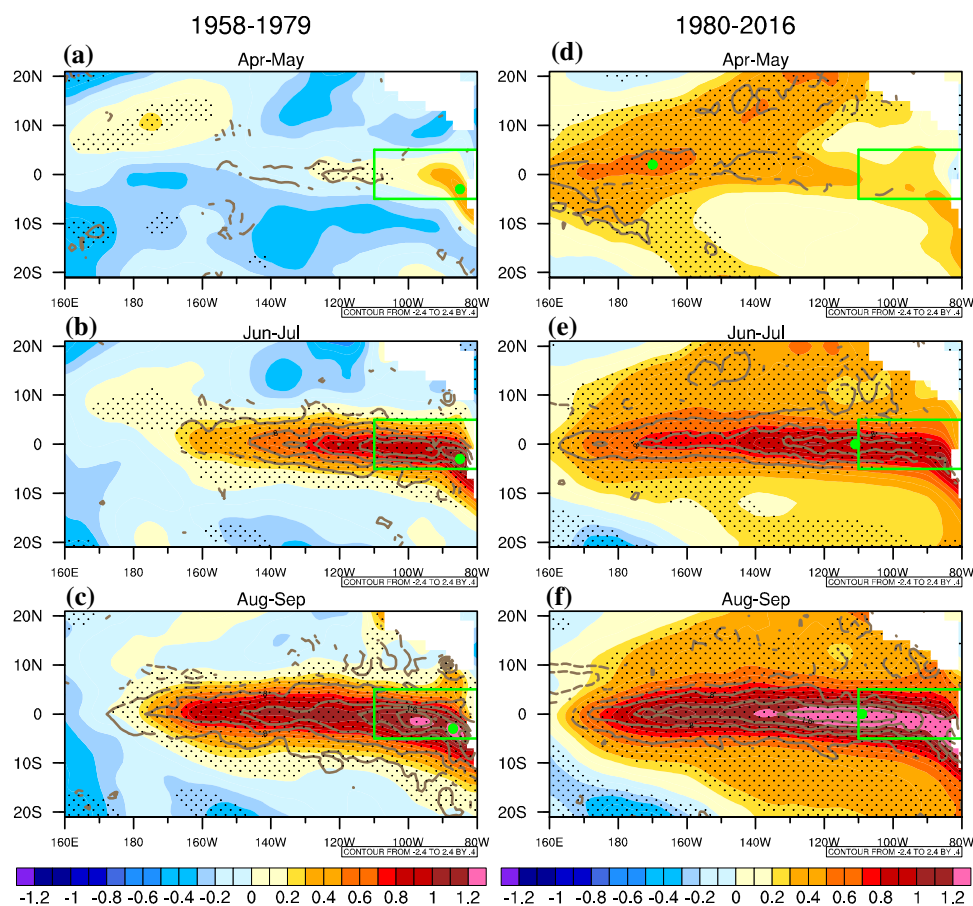
$$\beta V_s = \frac{curl \tau}{\rho H} \tag{7}$$

where ρ is the seawater density, H is the mean thermocline depth, τ is the wind stress, β is the planetary vorticity gradient, and V_s is the Sverdrup flow.

The difference of mean zonal wind stress averaged over $170^\circ W-90^\circ W$ between ID1 and ID2 is shown in right-top panel of Fig. 10. The maximum zonal wind stress difference appears near the equator and there is a cyclonic wind stress curl at north and south of the equator. According to Eq. (7), the cyclonic shear of wind stress would generate a northward (southward) Sverdrup transport in northern (southern) hemisphere, lifting the equatorial thermocline.

How does the aforementioned thermocline change influence the El Niño initiation? It is speculated that during ID1 the mean thermocline depth in the western and central Pacific was so deep that it prevented any significant SST changes in situ caused by interannual thermocline

Fig. 8 Evolution of SSTA (shading, with intervals of $0.1\text{ }^{\circ}\text{C}$) and MLTA (contour, with intervals of $0.4\text{ }^{\circ}\text{C}$) during the developing phase (April–September) of El Niño for 1958–1979 (left panel) and 1980–2016 (right panel). Green box indicates the budget diagnosis box. Green dots represent the maximum SSTA center. Black dots denote the SSTA pass the 90% bootstrap significance level. Contour shows MLTA that exceeds 90% bootstrap significance level



fluctuation. As a result, the thermocline fluctuation can only induce a detectable SSTA over the eastern equatorial Pacific where mean thermocline is shallow. In ID2, the mean thermocline depth in the western and central Pacific is relatively shallow so that a local SSTA can be induced by an interannual thermocline depth anomaly.

Another possible cause is the occurrence of stronger high-frequency (HF) wind variability in ID2 than in ID1. It has been shown that westerly wind events (WWEs) play an important role in triggering a strong El Niño by inducing a strong thermocline depth anomaly at the equator (e.g., Chen et al. 2017b). Figure 11 shows the difference of standard deviation (STD) of HF zonal surface wind (HF-U) and wind stress anomaly (HF-Taux). Both the surface wind and wind stress fields are 90-day high-pass filtered. Stronger zonal surface wind and wind stress variabilities appear in the tropical Pacific during ID2 than ID1, especially in ($10^{\circ}\text{ S}–5^{\circ}\text{ N}$, $150^{\circ}\text{ E}–180$). The STD of HF-U and HF-Taux averaged in the box in ID2 is larger than ID1 (Fig. 11c). Considering that El Niño may induce stronger HF winds, the STD of HF wind variability with El Niño years removed is also calculated (Fig. 11d), and the results are essentially same as those from all years calculation.

Therefore, it is concluded that stronger HF wind and wind stress variability appears in ID2 than ID1.

What causes the stronger HF-U and HF-Taux anomaly over the equatorial western Pacific? The difference of mean 850 hPa specific humidity field between ID2 and ID1 (Fig. 12a) shows that the mean specific humidity increased in ID2, particularly over the equatorial western Pacific. The vertical profile of the area averaged specific humidity difference field shows that maximum increase appears in lower troposphere (around 700 hPa, Fig. 12b). This moisture profile, along with more unstable vertical temperature profile, favors more unstable atmospheric stratification in ID2. As a result, stronger HF wind variability may develop in ID2.

To quantitatively measure the strength of WWEs, we use an accumulated WWE index (AWI) proposed by Chen et al. (2017b). AWI is obtained by integrating the HF wind stress anomaly over the equatorial western Pacific ($5^{\circ}\text{ S}–5^{\circ}\text{ N}$, $120^{\circ}\text{ E}–180$) for a given period each year. For the period of January–December, the average AWI in ID1 is 0.58 m s^{-1} and increases to 0.83 m s^{-1} in ID2, indicating a 43% increase. A 34% increase is obtained if one only considers the period of January–May. The result indicates that stronger wind variability appears in ID2 than ID1 regardless of which period is considered.

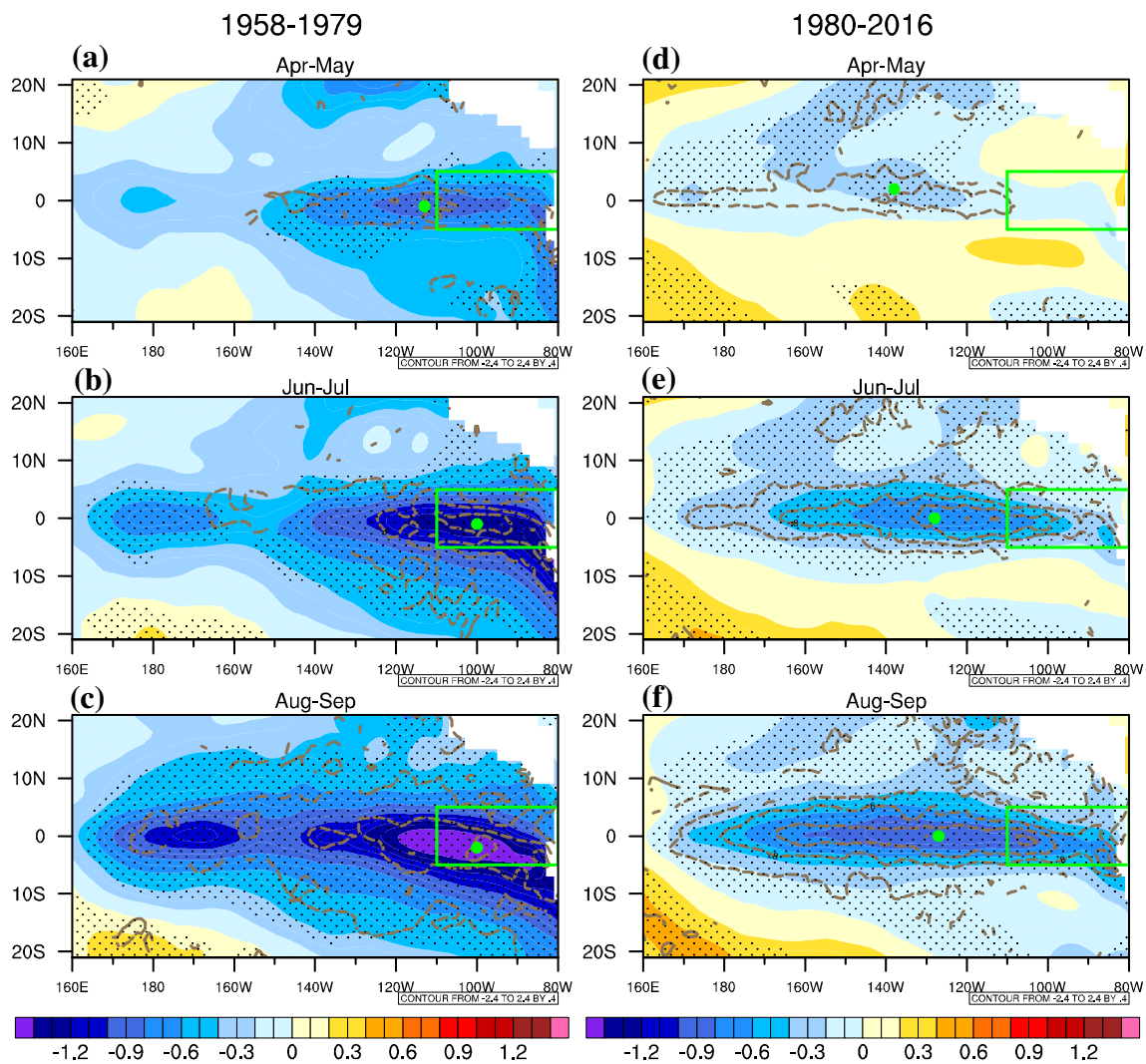


Fig. 9 As in Fig. 8 but is for La Niña in former period (left panel) and latter period (right panel), and green line box indicates the diagnosed box and green dot represents the minimum SSTA center

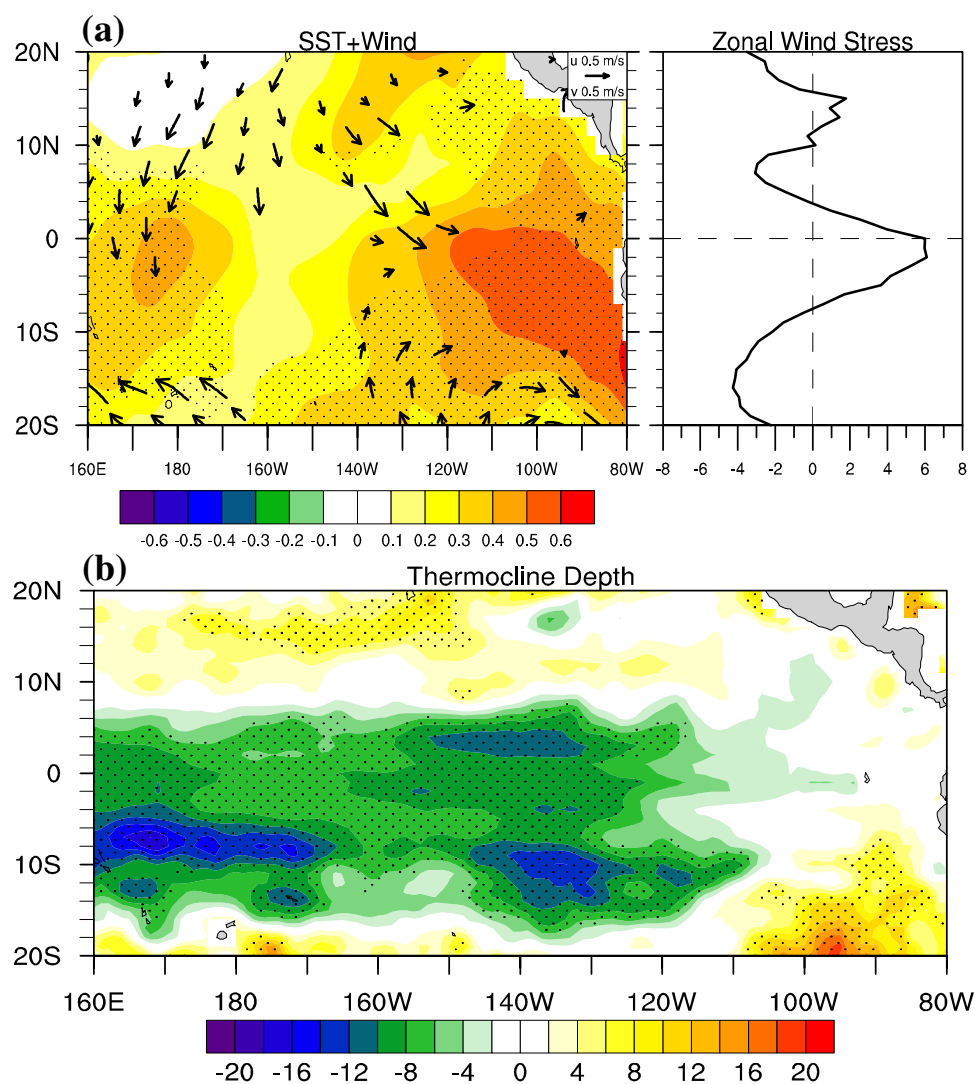
The enhanced HF wind variability may strengthen interannual thermocline fluctuation, as demonstrated by idealized oceanic general circulation model experiments (Chen et al. 2017b). Figure 13b shows the difference of STD of 2–7 years band-pass filtering thermocline depth anomaly. A stronger interannual thermocline depth variation (D') appeared in the equatorial western Pacific in ID2. The STD of D' averaged over (10°S – 5°N , 150°E – 180) increased by 27% in ID2. Therefore, more unstable atmosphere stratification in ID2 led to stronger HF-U variability, which induced stronger SST variability in the equatorial western-central Pacific through stronger thermocline variability.

The linkage between high-frequency wind disturbance and zonal location of atmosphere and ocean coupling has been pointed out by previous studies. For instance, Hu et al. (2012) suggested that a stronger and more eastward extended westerly wind activity along the equatorial Pacific in early

months of a year was associated with more active air-sea interaction over the cold tongue, which favoring the development of eastern Pacific El Niño.

To sum up, both the mean thermocline change and the high-frequency wind variability change favor the westward shift of El Niño initiation location. As a result, the initiation warming location shifts from the South American coast in ID1 to the western-central Pacific in ID2 (Fig. 8). But such mean state and high-frequency wind effects should affect both El Niño and La Niña. In fact, La Niña initiation locations also shifted westward in ID2 compared to ID1 (Fig. 9). The key difference lies in the distinctive initiation locations between El Niño and La Niña in ID1—A cold SSTA was initiated to the west of the green box (Fig. 9a), while a warm SSTA was initiated near South American coast (Fig. 8a). This difference led to distinctive nonlinear zonal advection signs between El Niño and La Niña in ID1 and thus the

Fig. 10 Difference of mean state from 1958–1979 to 1980–2016 (latter minus former) of a SST (shading; unit: $^{\circ}\text{C}$) and horizontal 850 hPa wind fields (vector; unit: m s^{-1}) and zonally averaged (170°W – 90°W) zonal wind stress (curve, unit: 10^{-3}N m^{-2}) and **b** thermocline depth (shading; unit: m). Dots denote the **a** SST and **b** thermocline depth difference fields exceeding the 90% significance level using t test. The vector only shows the meridional wind exceeding the 90% significance level



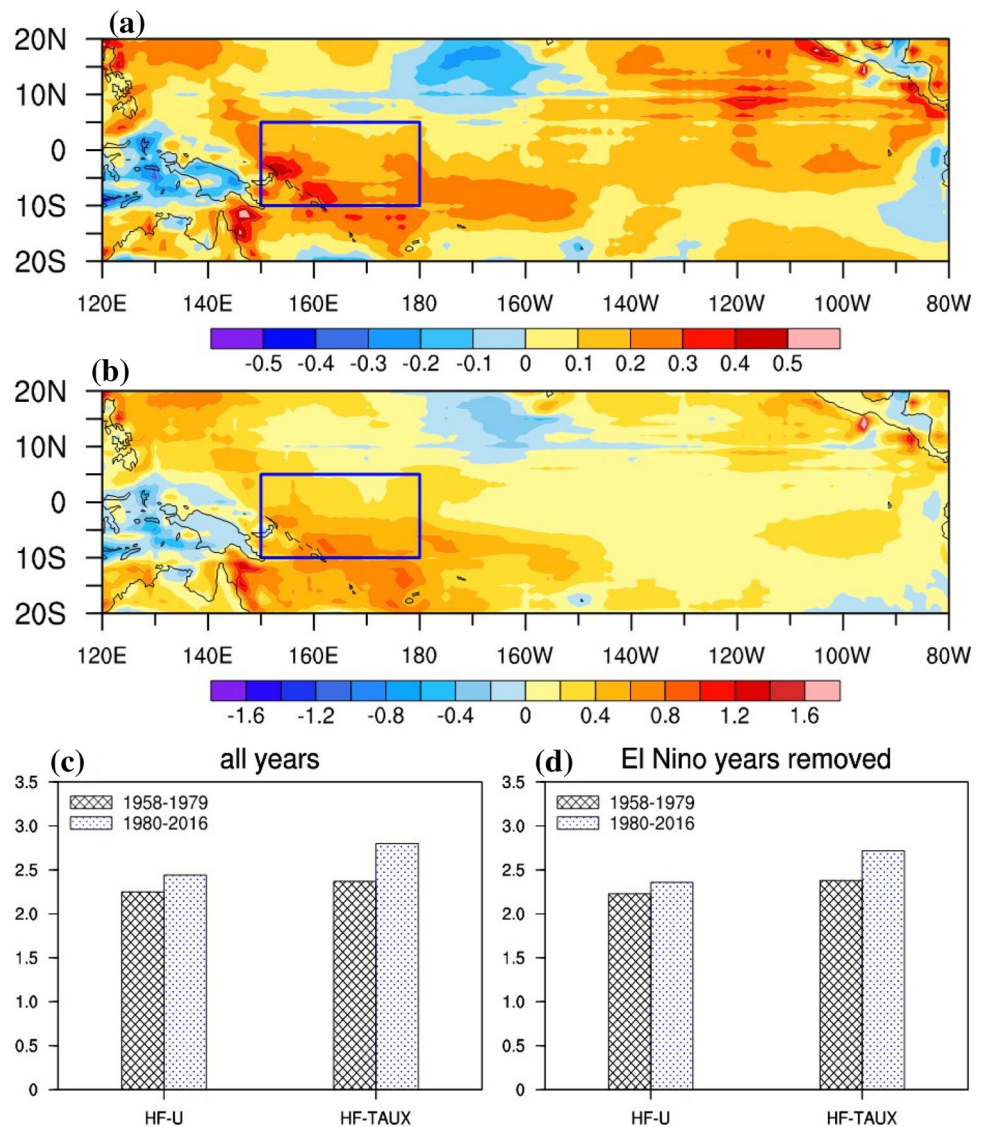
distinctive ENSO amplitude asymmetry evolutions between the two interdecadal periods.

What causes the different initiation location between El Niño and La Niña in ID1? We hypothesize that it was likely controlled by the longitudinal tilting of the climatological mean thermocline depth (Fig. 14). In the far eastern equatorial Pacific, the mean thermocline depth was so shallow that a further shoaling of the thermocline did not affect much of subsurface temperature below the mixed layer. As a result, SST change was not very sensitive to thermocline shoaling. However, it was very sensitive to the deepening of the thermocline, as the increase of thermocline depth would lead to a great increase of subsurface temperature, which, through mean upwelling, further affects surface temperature. This is why a positive SSTA was easily generated near the South American coast, while a negative SSTA appeared more frequently in the region a few hundred miles away from the coast where the mean thermocline is deeper compared to the coastal region but still shallower compared to

central equatorial Pacific. As a result, the initiation of a SST anomaly during La Niña appeared to the west of that of El Niño in ID1. The hypothesis above, however, requires further observational validation.

While the argument above emphasizes the importance of the mean state change in affecting ENSO behavior, one cannot rule out possibility that ENSO amplitude change may rectify the mean state change. For example, a simple theoretical model study by Jin et al. (2003) and a general circulation model study by Choi et al. (2009) pointed that ENSO might modify the mean state via oceanic nonlinear processes. A recent study by Capotondi et al. (2018) suggested that the power of low-frequency tail of high-frequency wind is a key to the ENSO variability. Further studies are needed to understand actual physical mechanisms behind the upscale feedback processes.

Fig. 11 Difference (ID2 minus ID1) of standard deviation (STD) of **a** high-frequency surface zonal wind (shading; unit: m s^{-1}) and **b** zonal wind stress (shading; unit: 10^{-2} N m^{-2}) anomaly fields. **c, d** Show the average standard deviation of high-frequency zonal surface wind and wind stress anomaly over the blue box region (10° S – 5° N , 150° E – 180) based on **c** all years and **d** all years except El Niño years



6 Conclusions

An observational analysis was conducted to reveal the interdecadal change of El Niño and La Niña amplitude asymmetry. It was found that the amplitude of El Niño and La Niña is approximately symmetric before 1980, but the amplitude of El Niño becomes significantly stronger than that of La Niña after 1980. A MK test shows that this change is statistically significant at the end of 1979. Thus two interdecadal periods (1958–1979 and 1980–2016) are separated to investigate physical processes that control the ENSO amplitude change respectively.

By diagnosing the oceanic mixed-layer heat budget, we found that the temperature tendency associated with dynamic and thermodynamic terms during El Niño and La Niña developing phase is similar before 1980. However, the tendency of El Niño is obviously stronger than that of La

Niña after 1980. The difference is primarily attributed to the ocean dynamics term. By further separating the dynamic term into linear and nonlinear advection terms, we found that the nonlinear advection, in particular the nonlinear zonal advection, was critical in causing the interdecadal change of ENSO amplitude asymmetry behavior. The nonlinear zonal advection term ($-u^i \frac{\partial T^i}{\partial x}$) was negative before 1980 but became positive after 1980. This led to a symmetric damping effect to El Niño and La Niña during ID1 but an asymmetric effect to El Niño and La Niña. As a result, a stronger El Niño but a weaker La Niña occurred during ID2.

It is found that anomalous geostrophic currents dominate surface zonal currents at the equator in both the periods. Positive (negative) thermocline depth anomalies during El Niño (La Niña) generate eastward (westward) geostrophic currents. While the center of the maximum SSTA during El Niño developing phase was confined to the South American

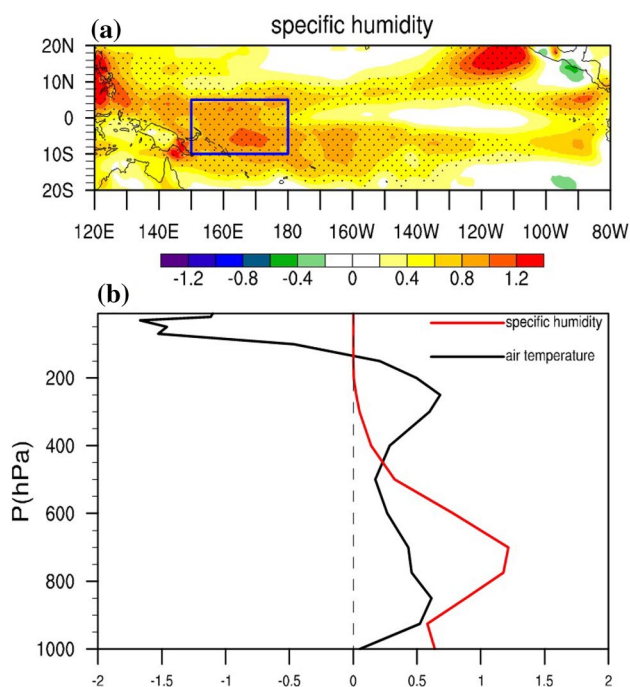


Fig. 12 **a** Difference (ID2 minus ID1) of mean 850 hPa specific humidity field (shading; unit: g Kg^{-1}) and dots denote the region exceeding the 90% significance level using t test; **b** vertical profiles (unit: hPa) of the mean specific humidity (red) and temperature (black; unit: $^{\circ}\text{C}$) difference (ID2 minus ID1) fields averaged over the blue box region (10°S – 5°N , 150°E – 180)

coast (east of 90°W) in ID1, it shifted westward to 110°W in ID2. Such a change was critical for generating a negative (positive) nonlinear zonal advection in ID1 (ID2). However, for La Niña, the maximum negative SSTA center always located to the west of the key diagnosis box so that the zonal nonlinear advection remained the same sign.

The different nonlinear zonal advection behaviors during El Niño were closely related to distinctive initial warming scenarios between ID1 and ID2. During ID1, initial warming started in April from the Pacific east coast. The SSTA center then shifted westward slightly and was confined in the far eastern equatorial Pacific (east of 90°W) during El Niño developing phase (from June to September). In contrast, an anomalous SSTA center firstly formed in the equatorial central Pacific (around 170°W) in ID2. It then shifted eastward to 110°W in the following months. It appears that the El Niño initiation location controls the subsequent evolution of the SSTA center. In contrast, a negative SSTA center during La Niña was initiated to the west of 110°W during both the interdecadal periods.

The cause of the distinctive initial warming locations between ID1 and ID2 is possibly attributed to the interdecadal change of the mean state at the equator. It is noted that the equatorial thermocline depth becomes shallower in the central equatorial Pacific in ID2. As a result, SSTA is more

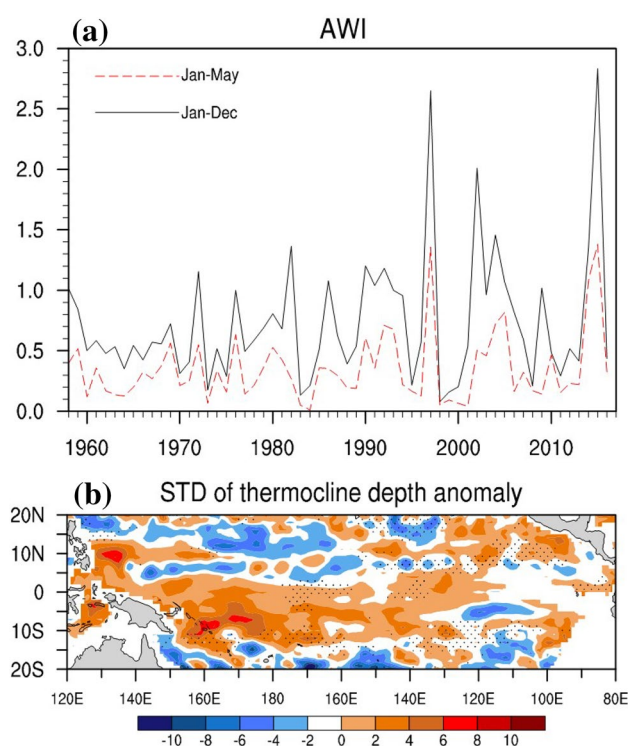


Fig. 13 **a** Time series of the accumulated WWE-index for the period of January–December (black) and January–May (red) each year. The difference of standard deviation (ID2 minus ID1) of 2–7 years band-pass filtering thermocline depth anomaly (shading, unit: m). Dots denote the area exceeding the 90% significance level using t test

sensitive to anomalous thermocline forcing in the central equatorial Pacific. Enhanced moisture and unstable atmosphere stratification in the western equatorial Pacific in ID2 may further invigorate high-frequency wind variability such as WWEs, which favor stronger thermocline and SST variability in situ. All these factors favor the westward shift of El Niño initiation location in ID2.

The change of the mean state and the high-frequency wind variability in ID2 also contributed to the westward shift of initiation location for La Niña. Therefore, the key difference that caused the asymmetric El Niño and La Niña amplitude evolutions lies in the distinctive initiation locations between El Niño and La Niña in ID1. We hypothesize that the difference is caused by the longitudinal tilting of the climatological mean thermocline depth. In the far eastern equatorial Pacific, the mean thermocline depth is so shallow that a further shoaling of the thermocline does not affect much change of subsurface temperature below the mixed layer. As a result, SST change is more (less) sensible to thermocline deepening (shoaling). This is why a positive SSTA was easily generated near the South American coast, while a negative SSTA appeared a few hundred miles away from the coast where the mean thermocline is deeper compared to the coastal region but shallower compared to central Pacific. As

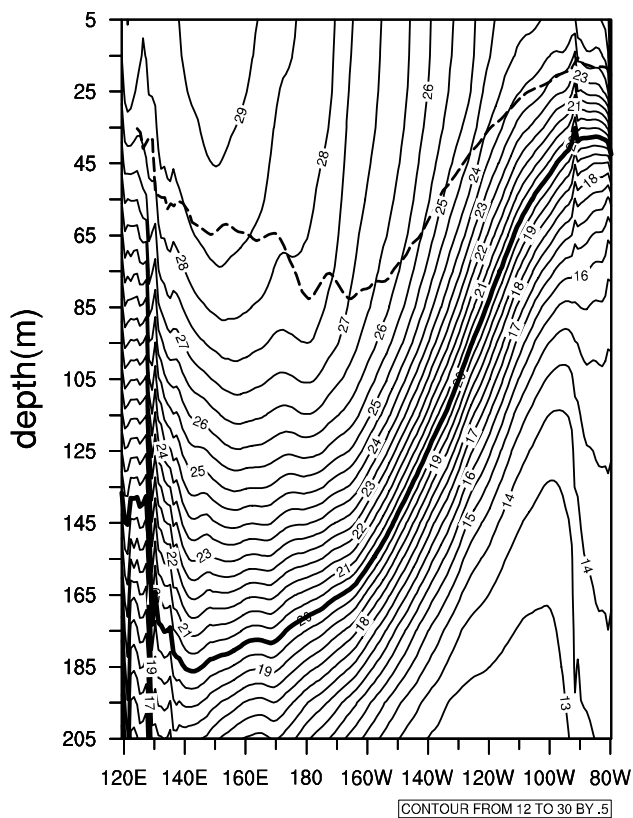


Fig. 14 The zonal-vertical distribution of climatological mean temperature (unit: °C, interval 0.5 °C) field averaged within 2° S–2° N during 1958–1979. A thick solid line is 20 °C isotherm representing the thermocline depth and a thick dashed line denotes the mixed-layer depth (which is defined as where the temperature is 0.5 °C lower than surface temperature)

a result, the initial cooling during La Niña appeared to the west of the initial warming during El Niño in ID1.

The hypothesis above, however, requires further observational validation and physical understanding. Through a quantitative diagnosis of mixed layer heat budget, we demonstrate the role of nonlinear zonal advection and initial warming/cooling location in affecting the ENSO amplitude asymmetry. While the fact that El Niño often initiated in the South America coast (western-central Pacific) prior to (after) 1980 has been well established by previous observational studies (e.g., Rasmusson and Carpenter 1982; Philander et al. 1984; Philander 1990), explaining its physical cause and applying it to the interdecadal change of ENSO amplitude asymmetry are, to our knowledge, of the first time. Thus, the current study provides a new physical linkage among the interdecadal mean state change, ENSO amplitude asymmetry, nonlinear zonal advection and initial warming/cooling location.

Acknowledgements This work was supported by NSFC Grants 41630423, NSF Grant AGS-15-65653, NOAA Grant NA18OAR4310298, and Jiangsu NSF grant BK20180811. This is

SOEST contribution number 10864, IPRC contribution number 1416, and ESMC contribution number 291.

References

- An SI (2004) Interdecadal changes in the El Niño–La Niña asymmetry. *Geophys Res Lett* 31:L23210
- An SI, Jin FF (2004) Nonlinearity and asymmetry of ENSO. *J Clim* 17(14):2851–2865
- An SI, Hsieh WW, Jin FF (2005) A nonlinear analysis of the ENSO cycle and its interdecadal changes. *J Clim* 18:3229–3239
- Battisti DS, Hirst AC (1989) Interannual variability in a tropical atmosphere–ocean model: influence of the basic state, ocean geometry and nonlinearity. *J Atmos Sci* 46(12):1687–1712
- Behringer DW (2007) The Global Ocean Data Assimilation System (GODAS) at NCEP. In: Preprints 11th Symp. on integrated observing and assimilation systems for atmosphere, oceans, and land surface, San Antonio, TX, Amer Meteor Soc, 3.3
- Bove MC, O’Brien JJ, Eisner JB et al (1998) Effect of El Niño on US Landfalling hurricanes, revisited. *Bull Am Meteorol Soc* 79(11):2477–2482
- Burgers G, Stephenson DB (1999) The “normality” of El Niño. *Geophys Res Lett* 26(8):1027–1030
- Cai W et al (2014) Increasing frequency of extreme El Niño events due to greenhouse warming. *Nat Clim Change* 4:111–116
- Cane MA, Zebiak SE (1985) A theory for El Niño and the Southern oscillation. *Science* 228(4703):1085–1087
- Capotondi A, Sardeshmukh PD, Ricciardulli L (2018) The nature of the stochastic wind forcing of ENSO. *J Clim* 31(19):8081–8099
- Carton JA, Giese BS (2008) A reanalysis of ocean climate using simple ocean data assimilation (SODA). *Mon Weather Rev* 136(136):2999–3017
- Carton JA, Chepurin G, Cao X et al (2000) A simple ocean data assimilation analysis of the global upper ocean 1950–95. Part I: methodology. *J Phys Oceanogr* 30(2):294–309
- Chang P, Wang B, Li T, Ji L (1994) Interactions between the seasonal cycle and the Southern Oscillation: frequency entrainment and chaos in an intermediate coupled ocean atmosphere model. *Geophys Res Lett* 21:2817–2820
- Changnon SA (1999) Impacts of 1997–98 El Niño Generated Weather in the United States. *Bull Am Meteorol Soc* 80(9):1819–1827
- Chen L, Li T, Yu Y (2015) Causes of strengthening and weakening of ENSO amplitude under global warming in four CMIP5 models. *J Clim* 28:3250–3274
- Chen L, Li T, Behera SK, Doi T (2016a) Distinctive precursory air-sea signals between regular and super El Niños. *Adv Atmos Sci* 33:996–1004
- Chen L, Yu Y, Zheng W (2016b) Improved ENSO simulation from climate system model FGOALS-g1.0 to FGOALS-g2. *Clim Dyn* 47:2617–2634
- Chen M, Li T, Shen X et al (2016c) Relative roles of dynamic and thermodynamic processes in causing evolution asymmetry between El Niño and La Niña. *J Clim* 29(6):2201–2220
- Chen L, Li T, Yu Y, Behera SK (2017a) A possible explanation for the divergent projection of ENSO amplitude change under global warming. *Clim Dyn* 49:3799–3811
- Chen L, Li T, Wang B, Wang L (2017b) Formation mechanism for 2015/16 super El Niño. *Sci Rep* 7:2975
- Chen L, Zheng W, Braconnot P (2019) Towards understanding the suppressed ENSO activity during mid-Holocene in PMIP2 and PMIP3 simulations. *Clim Dyn* 53(1–2):1095–1110
- Choi J, An SI, Dewitte B, Hsieh WW (2009) Interactive feedback between the tropical Pacific decadal oscillation and ENSO in a coupled general circulation model. *J Clim* 22:6597–6611

- Chung PH, Li T (2013) Interdecadal relationship between the mean state and El Niño types. *J Clim* 26(2):361–379
- Collins M et al (2010) The impact of global warming on the tropical Pacific and El Niño. *Nat Geosci* 3:391–397
- Compo GP, Whitaker JS, Sardeshmukh PD (2006) Feasibility of a 100-year reanalysis using only surface pressure data. *Bull Am Meteorol Soc* 87(2):175–190
- Dee DP, Uppala SM, Simmons AJ et al (2011) The era-interim reanalysis: configuration and performance of the data assimilation system. *Q J R Meteorol Soc* 137(656):553–597
- Dong B, Sutton RT, Scaife AA (2006) Multidecadal modulation of El Niño–Southern Oscillation (ENSO) variance by Atlantic Ocean sea surface temperatures. *Geophys Res Lett* 33:L08705
- Hong CC, Li T, Kug JS (2008) Asymmetry of the Indian Ocean dipole. Part I: observational analysis. *J Clim* 21(18):4834–4848
- Hu ZZ, Kumar A, Jha B et al (2012) An analysis of warm pool and cold tongue El Niños: air-sea coupling processes, global influences, and recent trends. *Clim Dyn* 38(9–10):2017–2035
- Huang R, Wu Y (1989) The influence of ENSO on the summer climate change in China and its mechanism. *Adv Atmos Sci* 6(1):21–32
- Huang B, Xue Y, Zhang D et al (2010) The NCEP GODAS ocean analysis of the tropical Pacific mixed layer heat budget on seasonal to interannual time scales. *J Clim* 23(18):4901–4925
- Jin FF (1997) An equatorial ocean recharge paradigm for ENSO. Part I: Conceptual model. *J Atmos Sci* 54(7):811–829
- Jin FF, An SI, Timmermann A et al (2003) Strong El Niño events and nonlinear dynamical heating. *Geophys Res Lett* 30(3):201–204
- Kanamitsu M, Ebisuzaki W, Woollen J et al (2002) NCEP–DOE AMIP-II reanalysis (R-2). *Bull Am Meteorol Soc* 83(11):1631–1643
- Kang IS, No HH, Kucharski F (2014) ENSO amplitude modulation associated with the mean SST changes in the tropical central Pacific induced by Atlantic multidecadal oscillation. *J Clim* 27:7911–7920
- Kirtman BP, Schopf PS (1998) Decadal variability in ENSO predictability and prediction. *J Clim* 11(11):2804–2822
- Kumar A, Hu ZZ (2012) Uncertainty in the ocean-atmosphere feedbacks associated with ENSO in the reanalysis products. *Clim Dyn* 39(3–4):575–588
- Li T (1997) Phase transition of the El Niño–Southern Oscillation: a Stationary SST Mode. *J Atmos Sci* 54(54):2872–2887
- Li T, Hsu PC (2017) ENSO dynamics. *Fundamentals of tropical climate dynamics*. Springer International Publishing, Cham, p 236
- Li T, Zhang Y, Lu E, Wang D (2002) Relative role of dynamic and thermodynamic processes in the development of the Indian Ocean dipole: an OGCM diagnosis. *Geophys Res Lett* 29:25–21–25–24
- Li T, Wang B, Wu B et al (2017) Theories on formation of an anomalous anticyclone in Western North Pacific during El Niño: a review. *J Meteorol Res* 31(6):987–1006
- Li X, Hu ZZ, Huang B (2019) Contributions of atmosphere-ocean interaction and low-frequency variation to intensity of strong El Niño events since 1979. *J Clim* 32(5):1381–1394
- McPhaden MJ, Zebiak SE, Glantz MH (2006) ENSO as an integrating concept in earth science. *Science* 314(5806):1740–1745
- Neelin JD, Battisti DS, Hirst AC et al (1998) ENSO theory. *J Geophys Res Oceans* 103(C7):14261–14290
- Okumura YM, Deser C (2010) Asymmetry in the duration of El Niño and La Niña. *J Clim* 23(21):5826–5843
- Okumura YM, Sun T, Wu X (2017) Asymmetric modulation of El Niño and La Niña and the linkage to tropical Pacific decadal variability. *J Clim* 30:4705–4733
- Philander SG (1990) *El Niño, La Niña, and the Southern Oscillation*. Academic Press, London, p 289
- Philander SGH, Yamagata T, Pacanowski RC (1984) Unstable air-sea interactions in the tropics. *J Atmos Sci* 41(4):604–613
- Picaut J, Masia F, Penhoat YD (1997) An advective-reflective conceptual model for the oscillatory nature of the ENSO. *Science* 277(5326):663–666
- Rasmusson EM, Carpenter TH (1982) Variations in Tropical Sea Surface Temperature and Surface Wind Fields Associated with the Southern Oscillation/El Niño. *Mon Weather Rev* 110(5):354–384
- Rodgers KB, Friederichs P, Latif M (2004) Tropical Pacific decadal variability and its relation to decadal modulations of ENSO. *J Clim* 17:3761–3774
- Ropelewski CF, Halpert MS (1987) Global and regional scale precipitation patterns associated with the El Niño/Southern oscillation. *Mon Weather Rev* 115:1606–1626
- Smith TM, Reynolds RW, Peterson TC et al (2008) Improvements to NOAA's historical merged land-ocean surface temperature analysis (1880–2006). *J Clim* 21(10):2283–2296
- Su JZ, Zhang RH, Rong XY et al (2010) Causes of the El Niño and La Niña amplitude asymmetry in the equatorial eastern Pacific. *J Clim* 23(3):605–617
- Suarez MJ, Schopf PS (1988) A delayed action oscillator for ENSO. *J Atmos Sci* 45(21):3283–3287
- Uppala SM, Kallberg PW, Simmons AJ et al (2005) The ERA-40 reanalysis. *Q J R Meteorol Soc* 131(612):2961–3012
- Wallace JM, Gutzler DS (1981) Teleconnections in the geopotential height field during the Northern Hemisphere winter. *Mon Weather Rev* 109(4):784–812
- Wang B, An SI (2001) Why the properties of El Niño changed during the late 1970s. *Geophys Res Lett* 28(19):3709–3712
- Wang B, Wu R, Fu X (2000) Pacific–East Asian teleconnection: how does ENSO affect east Asian climate? *J Clim* 13(9):1517–1536
- Wang B, Wu R, Li T (2003) Atmosphere–warm ocean interaction and its impacts on Asian–Australian Monsoon variation. *J Clim* 16:1195–1211
- Weisberg RH, Wang C (1997) A Western Pacific oscillator paradigm for the El Niño–Southern Oscillation. *Geophys Res Lett* 24(7):779–782
- White GH (1980) Skewness, kurtosis and extreme values of northern hemisphere geopotential heights. *Mon Weather Rev* 108(9):1446–1455
- Wu B, Li T, Zhou TJ (2010) Asymmetry of atmospheric circulation anomalies over the western North Pacific between El Niño and La Niña. *J Clim* 23(18):4807–4822
- Wu B, Zhou TJ, Li T (2017) Atmospheric dynamic and thermodynamic processes driving the western North Pacific anomalous anticyclone during El Niño. Part I: maintenance mechanisms. *J Clim* 30:9621–9635
- Xiang B, Wang B, Li T (2013) A new paradigm for the predominance of standing central Pacific warming after the late 1990s. *Clim Dyn* 41(2):327–340
- Xue Y, Smith TM, Reynolds RW (2003) Interdecadal changes of 30-Yr SST normals during 1871–2000. *J Clim* 16(10):1601–1612
- Yeh SW, Kirtman BP (2004) Tropical Pacific decadal variability and ENSO amplitude modulation in a CGCM. *J Geophys Res* 109:C11009
- Yeo SR, Yeh SW, Kim KY et al (2016) The role of low frequency variation in the manifestation of warming trend and ENSO amplitude. *Clim Dyn* 49(4):1197–1213
- Zhu ZW, Li T (2016) A new paradigm for continental US summer rainfall variability: Asia–North America teleconnection. *J Clim* 29:7313–7327
- Zhu ZW, Li T (2018) Amplified contiguous United States summer rainfall variability induced by East Asian monsoon interdecadal change. *Clim Dyn* 50(9–10):3523–3536

Publisher's Note Springer Nature remains neutral with regard to jurisdictional claims in published maps and institutional affiliations.